Flow transitions on a cambered airfoil at moderate Reynolds number

Cite as: Phys. Fluids **33**, 093105 (2021); https://doi.org/10.1063/5.0061939
Submitted: 30 June 2021 . Accepted: 01 September 2021 . Published Online: 15 September 2021

J. D. Tank, B. F. Klose, G. B. Jacobs, et al.

Physics of Fluids ARTICLE scitation.org/journal/phf

Flow transitions on a cambered airfoil at moderate Reynolds number

Cite as: Phys. Fluids 33, 093105 (2021); doi: 10.1063/5.0061939
Submitted: 30 June 2021 · Accepted: 1 September 2021 ·
Published Online: 15 September 2021

J. D. Tank,[1] B. F. Klose,[2] G. B. Jacobs,[2] and G. R. Spedding[1,a)]

AFFILIATIONS

[1]University of Southern California, Los Angeles, California 90089-1191, USA
[2]San Diego State University, San Diego, California 92182-1308, USA

Note: This paper is part of the special topic, Tribute to Frank M. White on his 88th Anniversary.
[a)]Author to whom correspondence should be addressed: geoff@usc.edu

ABSTRACT

A combined experimental and numerical study is performed to investigate the flow field and associated aerodynamic forces on a cambered airfoil. The Reynolds number is low enough to ensure importance of viscous dynamics, and high enough so that instability and transition to turbulence can occur. The flow fields are complex and their correct description is essential in understanding the nonlinear curves describing the variation of lift and drag coefficients with angle of attack, α. As α is increased from 0, the flow states go through a number of qualitatively distinct phases. At low to moderate α, the laminar boundary layer separates before the trailing edge, and as the separation point moves forward, instabilities of the detached shear layer form coherent vortices over the upper (suction) surface. At a critical angle, α_{crit}, instabilities in the shear layer grow fast enough to transition to turbulence, which then leads to reattachment before the trailing edge. In this flow state, lift is increased and drag decreases. Hence, in order to understand the aerodynamics at this scale, we need to understand the viscous dynamics of the boundary layer, as elegantly described and analyzed by Frank White.

I. INTRODUCTION

In his monograph/textbook *Viscous Fluid Flow*,[1] Frank White argues that the biggest breakthrough in practical fluids engineering came from Prandtl's demarcation of a flow into two parts: one being a thin boundary layer to which viscous effects are confined and an outer flow where the elegant mathematics of inviscid solutions could be pursued. Such a partition forms the basis of almost all practical aeronautics, enabled by the fact that characteristic speeds U and length scales L in air are such that Reynolds numbers, $Re = UL/\nu$ ($\nu = \rho/\mu$ is the kinematic viscosity) take on values of 10^6 or more. That is no longer the case as problems in design of flight vehicles at small scales and/or high altitudes lead to significant interest in lower Re domains. Paradoxically, the decrease in speeds and length scales of interest now makes the fluid mechanics potentially much more complex, with greatly increased sensitivity to geometry and atmospheric variations. Previously routine prediction and measurement of airfoil and wing performance become more difficult as Re_c (where the chord length c is used for L; we follow this aeronautical convention and drop the c-subscript) falls below 10^5. The thorough documentation of wind tunnel tests by Selig and colleagues[2–6] demonstrated quite clearly how lift: drag polars developed non-monotonic behavior at low Re, and how tests from different facilities could report different results from nominally identical conditions. Further wind tunnel tests[7–10] on specific airfoil geometries for specific applications showed that both testing and airfoil design at these low Re were complicated by non-negligible viscous effects, and among these are the development of complex coherent structures that can form and influence the global flow (e.g., Ref. 11). The comment in Ref. 12 that the aerodynamic performance is strongly influenced by the properties of the viscous boundary layer, in particular by its comparatively poor resistance to separation, has been borne out in practice many times. There is a range of Re, approximately from 10^4 to 10^5, where the laminar boundary layer always separates within one chord length but where instabilities of the separated shear layer may have growth rates large enough for transition to turbulence, when the flow may reattach in a time-averaged sense. The region between separation and reattachment is termed a laminar separation bubble (LSB). The dynamics of the LSB are affected by an array of two- and three-dimensional instabilities and also by upstream propagation of acoustic modes originating from vortex shedding at the trailing edge. The detailed dynamics of the LSB have been investigated in experiment[13–15] and in computations either in DNS[16–18] or with a Large Eddy Simulation.[19,20]

At moderate Re (as defined above), the transition from laminar separated flow to a transitional flow resulting in an LSB can lead to sudden (over 1° in α) and significant changes in integrated aerodynamic force coefficients. Denoting the state of laminar separation without reattachment SI and reattachment following LSB formation SII, experiments on the Eppler 387 airfoil at moderate Re showed that the SI–SII transition could lead to increases in L/D of greater than 40%, through increase in L and decrease in D.[21] The changes in L/D could be achieved in SI–SII transitions forced through active or passive control measures,[22–24] thereby exploiting the intrinsic sensitivities of the separation-prone boundary layer. Abrupt changes in c_l have notably been documented in Ref. 8 at $Re = 4 \times 10^4$ on a NACA (National Advisory Committee for Aeronautics) 66–018 airfoil, and the force coefficients were strongly affected by acoustic excitation at a particular frequency. The production and amplification of Kelvin–Helmholtz spanwise vortices have been described in further detailed experiments[11,25–28] where the dependence of roll-up location on both Re and α has been discussed.

Because the global flow is ultimately determined by the viscous conditions at suction surface, a number of detailed experimental and computational studies have focused on the LSB itself in experiments where the stable LSB is an integral part of a specially designed airfoil (e.g., Refs. 14 and 15) and in simulations, either of the naturally occurring bubble on a standard NACA 0012 shape[16,17,19] or of a model problem where the LSB is induced through a pressure gradient imposed on a flat plate.[29,30] At the same time, determining both details within the boundary layer and resolving the global airfoil/wing-induced flow field are challenging both experimentally and computationally. True direct numerical simulations that resolve all scales including those of turbulence post-transition are expensive and performed at select parameter values (Re, α) only. Though there is interest in how model computations (LES, RANS) may be used to simulate these flows at much less expense (c.f.[20,31]), the computations here are fully resolved. Corresponding or equivalent experiments require very low turbulence facilities and careful attention to details of geometry, model vibration, and support.

Here, we report on a program of combined DNS and experimental studies on a NACA 65-412 airfoil, which is a cambered profile found in turbine blades, among other applications. At $Re = 2 \times 10^4$, the DNS resolves all scales and equivalent experiments at matching Re can be run in both wind tunnel and water channel facilities. Water channels have higher ambient turbulence levels than wind tunnels, but slower flow speeds and larger length scales allow fine scale features to be found through dye visualization, as dye traces can mark thin filaments that would not be revealed in a spatially averaged measure. The objective is to show how the aerodynamic performance characteristics of a practical airfoil can be traced back to their viscous fluid flow and ensuing complex coherent structures and instabilities at the boundary. Since the flow solutions in all cases are governed by the viscous Navier–Stokes equations, a secondary purpose is to identify how and when differences in measured quantities may yet be found.

II. MATERIALS AND METHODS

A. Wind tunnel and models

PIV and force balance tests were run in the octagonal test section of the Dryden Wind Tunnel (DWT), (1.37 m span, $T < 0.035\%$ for disturbances between 10 Hz $< f <$ 1000 Hz), as shown in Fig. 1. All models were milled from aluminum using a CNC mill with a precision of 0.0127 mm. As the wings are used in PIV experiments, the final finish is a light sanding from a matt black spray-painted covering. The wing models used in the PIV tests had the following dimensions: $c = 0.075$ m and $b = 0.225$ m, for $AR = b/c = 3$. All tests reported here are for a nominally two-dimensional configuration where a rectangular wing is set between end plates. The end plates taper to a point in the upstream direction, 20 cm in front of the wing leading edge. If the laminar boundary layer thickness on the plate is

$$\delta = \frac{5.2x}{\sqrt{Re_x}}, \tag{1}$$

then at $U = 4$ m/s, $\delta = 4.5$ mm and the maximum gap width between the plate and wing is 1 mm $= 0.22\delta$. The force balance tests were performed on models with $AR = 3$ and $AR = 12.9$ ($c = 0.055$ m, $b = 0.71$ m). The larger AR (and area) model was sized to generate forces that could be measured most accurately with the DWT force balance at $Re = 2 \times 10^4$. Time-averaged lift and drag curves generated with both models could be compared at $Re = 4 \times 10^4$, where both models generated forces in an appropriate range for the balance. The sum of corrections for model and wake blockage and for streamline curvature[2,32] were estimated as less than 2% for all models.

B. Particle imaging velocimetry (PIV)

During PIV tests, the tunnel was filled with glycerin-based smoke and a laser sheet parallel to the flow direction (in $\{x, z\}$) was generated by a double-pulsed Nd:YAG laser. A digital camera (1600 × 1200 pixel, 14 bit) imaged particle fields on a cross section at mid-span ($y = 0$) through a Nikon 70–210 mm f/4–5.6 NIKKOR AF lens. Two wing models that were mirror images of each other were used to collect data over both the pressure and suction surfaces of the airfoil. α was set by alignment with a row on the digital image array, with an estimated uncertainty of 0.2°.

In order to increase spatial resolution, the flow field was split into either five (for $\alpha = [0°, 2°, 4°, 6°, 8°$, and $10°]$) or two (for $\alpha = [10°, 10.1°, 10.2°, 10.3°, 10.4°, 10.5°]$) overlapping sub-regions. When two sub-regions are used, they correspond to the forward and the aft sections of the suction side of the airfoil, and are closely focused on the airfoil alone, with no coverage of the incoming flow, or of the wake. The more general views require larger number of five panels. When five sub-regions are used to image the larger field of view, they correspond to the forward and aft sections of both the suction and the pressure sides of the airfoil, and the wake. 1000 image pairs were captured for each sub-region at a sampling rate of 9.6 Hz. This sampling rate was not sufficient to provide time-resolved data, but did allow for the generation and analysis of time-averaged and instantaneous flow fields. The images were processed with LaVision/DaVis to produce velocity field estimates (u, w) on a uniform grid using a multi-pass algorithm, which had interrogation windows that were reduced to 16 × 16, 8 × 8, or 6 × 6 pixels for the final pass. A 50% interrogation box overlap gave a final spatial resolution of[3,4,8] pixels, which is [0.11, 0.14, 0.28] mm. This corresponds to $[0.08, 0.11, 0.21] \times \delta_{lam}$ or $[0.06, 0.07, 0.15] \times \delta_{turb}$, where $\delta_{lam} = \frac{5x}{\sqrt{Re}}$ and $\delta_{turb} = \frac{0.37x}{Re^{\frac{1}{5}}}$ are the laminar and turbulent boundary layer thickness, respectively, at $0.5c$ of a flat plate with the same chord length as the model used.

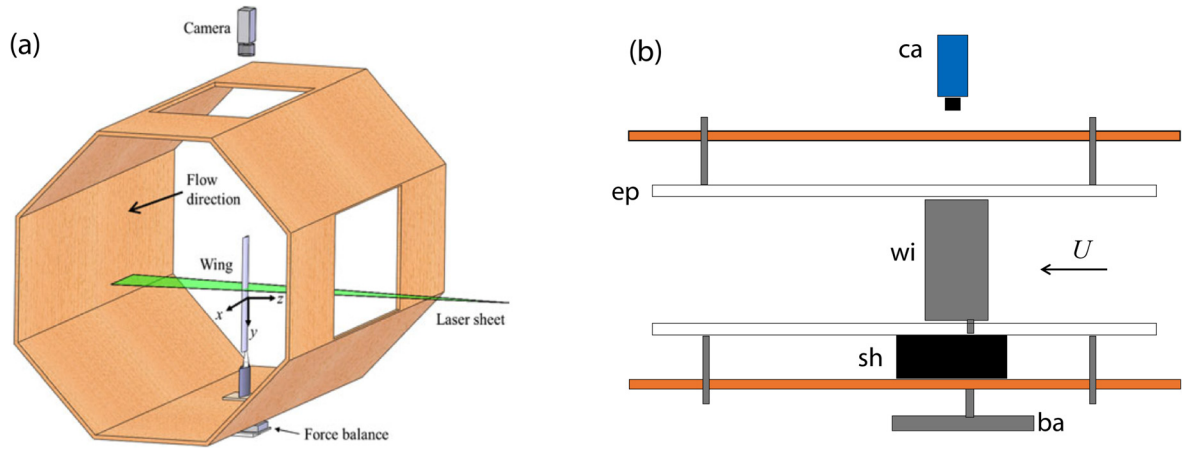

FIG. 1. (a) Tunnel test section geometry and generic wing, lighting, and camera arrangement. (b) In 2D experiments, the wing (w) is placed between two end plates (ep), and a shroud (sh) covers the balance sting from one wall to the nearest end plate. The upstream ends of the end plates taper to a point.

Unlike their usual aeronautical counterparts at higher *Re*, flow fields about the wing section are very strongly influenced by the viscous boundary layer and associated separation, and the PIV acquisition parameters are driven mainly by attempts to resolve these regions. For a given illumination and seeding density, the effective PIV exposure time, δt, is the most critical parameter. If $\delta t = 100$ μs, then for $U = 1$ m/s (toward the edge of the boundary layer), one expects a displacement $U\delta t$ of 0.1 mm, which is half the smallest correlation box size of 6 pixels. The outer flow, $U = 4$ m/s gives a displacement of 24 pixels, and can be resolved with a fixed pixel shift of 12 pix on an initial coarse grid of 32^2 correlation boxes. The same coarse grid can accommodate a 0 pix shift close to the wall. Subsequent correlation box size reductions use initial displacements as the search origin and allow for successive refinement down to the extreme of 6×6 pix boxes. The procedure followed was to begin with a nominal $\delta t = 100$ μs and then to increase or decrease it as conditions dictate. In practice, each α has a different δt which would range from 60 to 120 μs, depending on the flow topology and complexity. Part of the flow complexity comes from three-dimensional motions that bring fluid into and out of the laser sheet. The sheet thickness is approximately 2 mm on the wing surface, which is almost 10 times larger than the best in-plane resolution.

Each velocity field $\{u, w\}(x, z)$ can be interpolated and smoothed using a smoothing spline function,[33] and the spatial derivatives can be computed from the spline coefficients themselves, thus removing the grid spacing as a source of error in the gradient estimation, and the spanwise vorticity is

$$\omega_y = \frac{\partial w}{\partial x} - \frac{\partial u}{\partial z}. \tag{2}$$

The degree of smoothing is a free parameter and is selected here so that no fluctuations in velocity profiles remain that are composed of four or fewer data points. Such a limit reduces common algorithmically generated sources of error such as peak-locking, and the largest remaining sources of error are through the in-plane shear, *S*, and through particles moving out of the light sheet through the velocity component *v*.[34] This is the best way to retain proper amplitudes of small-scale vorticity distributions, and is used for all instantaneous velocity field data. Here, we mostly compare the structure of time-averaged velocity and vorticity fields and a much less time-consuming procedure is then to average all 1000 snapshots to yield one time-averaged velocity field, $(\bar{u}, \bar{w})$, for each sub-region of the flow. These subregions are then interpolated on the Matlab thin-plate spline function tpaps, which are used to estimate the time-averaged spanwise vorticity, $\bar{\omega}_y = \frac{\partial \bar{w}}{\partial x} - \frac{\partial \bar{u}}{\partial z}$. The sub-region velocity/vorticity fields were finally combined to form one composite velocity/vorticity field for each α.

C. Force measurements

Force measurements were performed with a custom, three-component force balance (Fig. 2),[35] which measures forces normal and tangent to the chord of the wing. The balance rotates around with the wing as α varies, and the forces were converted to lift and drag, defined with respect to the freestream, as conventional. The lift and drag forces were then expressed as the usual dimensionless quantities as follows:

$$c_l = \frac{L}{qS}, \tag{3a}$$

$$c_d = \frac{D}{qS}, \tag{3b}$$

where the lift and drag are normalized by the planform area, *S*, of the nominally two-dimensional model and $q = 1/2(\rho U^2)$ is the dynamic pressure.

A new balance calibration was performed before each test, generating a 3×4 calibration matrix, where the 3×3 load matrix is augmented with a zero offset column. The off-diagonal coefficients were typically two orders of magnitude smaller than the leading diagonal terms. The balance voltage outputs were passed through an analog op-amp and signal conditioner before sampling in a 14-bit ADC. The effective number of bits due to oversampling of the electrically noisy signal was 20,[21,36] which yields a baseline resolution of less than 0.02 mV over ± 10 V range. Based on calibrations and measurements

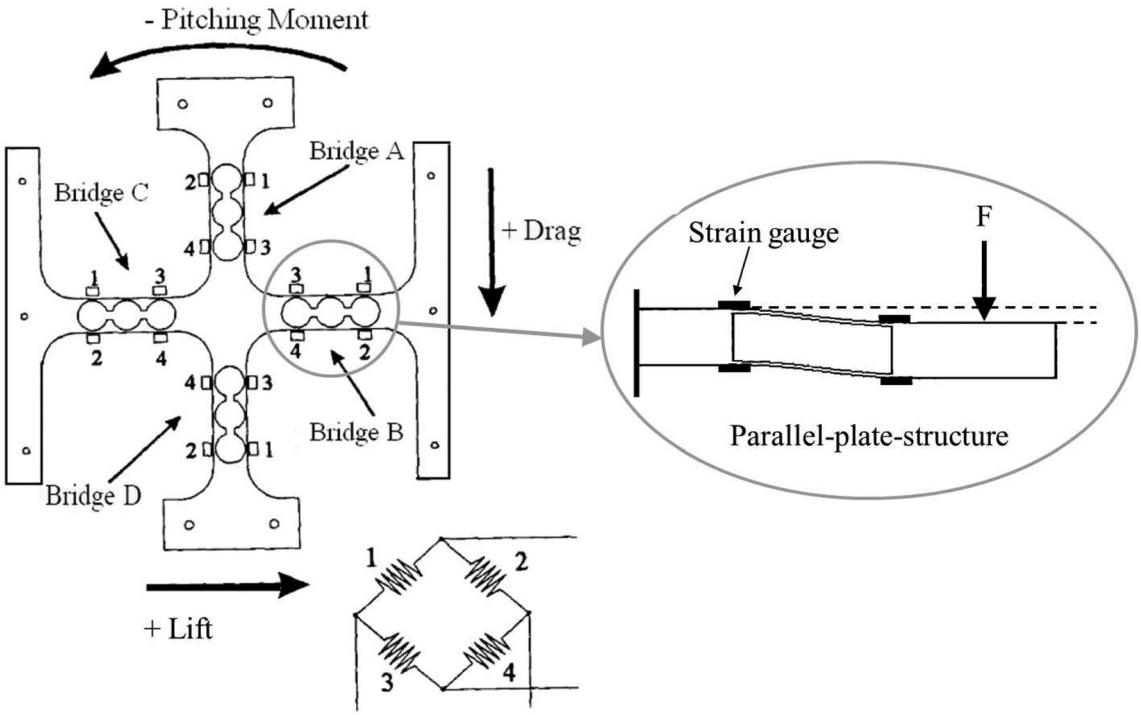

FIG. 2. Cruciform force balance. Each arm has strain gauges 1-2 and 3-4 in tension–compression arrangement to make up the four arms of a Wheatstone bridge. There are four bridges, one on each arm. From Ref. 35.

at typical loading conditions, the measurement uncertainty is less than 5 mN for forces tangent to the chord of the wing. The measurement uncertainty for forces normal to the chord of the wing is less than 15 mN for the same force range. $c_{d,min} = 0.03$ for the smallest wing would yield $D = 0.17$ N for a worst case relative uncertainty of 3%.

Each time-averaged force balance test consisted of five sweeps, forward and backward, through the entire α range in increments of 0.5°. After each α step, the flow was allowed to settle for ten seconds before ten seconds of data were collected at 5 kHz and averaged. The five sweeps produced ten time-averaged measurements for each α, which were averaged to obtain a single time-averaged value. This collection is reasonable if there is no hysteresis so forward and backward α-traverses give equivalent values. The lack of hysteresis (which varies with Re and AR) was verified over most conditions reported here. The uncertainty of each combined time-averaged force value was taken as the standard deviation of the ten time-averaged measurements. The entire test procedure was repeated at least three times to test for day-to-day repeatability.

D. Water channel flow visualization

Dye-injection flow visualization tests were carried out on a scaled model in the USC water channel (BWC, Fig. 3) which has a rectangular test section (L, W, $H = 762$, 89, 61 cm). Freestream velocity data were collected during tests with a MSE 2D miniLDV laser Doppler velocimeter, and $T < 1.7\%$ for all tests. These turbulence levels, though reasonable for a water channel, are about 50 times the wind tunnel levels.

The airfoil model was made of clear acrylic with $c = 14.4$ cm, $b = 45$ cm ($AR = 3.1$). This AR is sufficient to generate a largely two-dimensional flow at the mid-span location when tip vortices are blocked by the bottom of the channel at one end and an end plate positioned just beneath the free surface. Dye was injected from a leading-edge exit port at $y/b = 0$ and/or at various offset (in $\{x, z\}$)

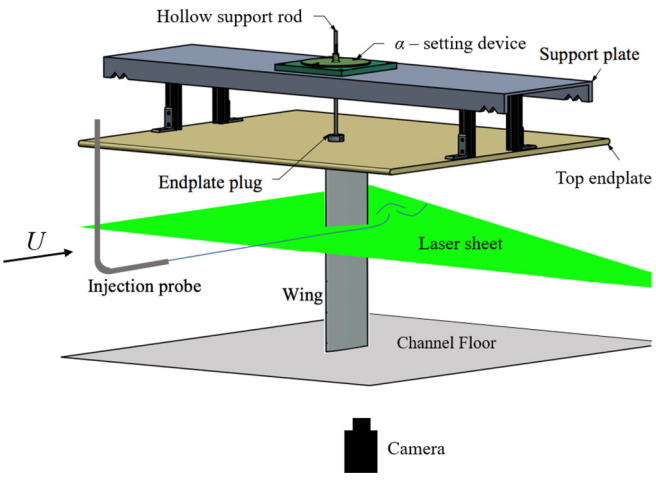

FIG. 3. Flow visualization setup in the water channel. The top end plate lies just beneath the water surface. The hollow support rod carries dye to injection ports at the leading edge, and dye can also be introduced upstream.

locations upstream. Dye materials were milk and alcohol (mixed for neutral buoyancy) or fluorescein/rhodamine complexes. A 5.14 W, 532 nm wavelength CNI continuous wave laser was spread into a sheet in an (x, z)-plane and aligned in the y-direction with the injection location to illuminate the dye. A Mako U-130 camera (1280×1024 pix, 10 bit) with an Edmund Optics 25 mm C series fixed focal length lens collected images at a frame rate of 20 fps from below the model through a window in the bottom of the channel. For $Re = 2 \times 10^4$, $U = 14$ cm/s, and a convection time c/U is on the order of 1 s, so sampling two orders of magnitude faster can be considered time-resolved for this flow. The second advantage of dye visualization is that fine scale features can be observed and traced that are lost in an average PIV correlation box. We may note that dye traces are Lagrangian markers, as particles are followed in time from their origin (either in the boundary layer, or upstream). Intricate patterns are accumulated time histories of the marked fluid, and their correspondence with Eulerian measures can be non-obvious.

E. Vortex shedding frequency

Flow visualization images of the airfoil wake ($1 < x/c < 2$), captured in the BWC, were analyzed using a Matlab script to estimate the wake vortex shedding frequency as a function of α. Dye injected into the boundary layer marks these structures, and so the images were analyzed to determine how often patches of dye passed through the wake. This was done by selecting a grid of pixels (20×20 pix) from an interrogation box in the wake images and determining their intensity as a function of time (Fig. 4). A spike in the intensity occurs when a patch of dye (i.e., vortex structure) passes over the pixel. A Fourier transform was then used to generate an amplitude spectrum for each pixel, and the spectra from all pixels on the grid were averaged to determine the dominant frequencies in the wake. This method generally produced sharp, distinct peaks at low α, where vortices could be clearly identified, but less distinct peaks at higher α, where the wake became more turbulent, leading to the diffusion of dye streaks. When there was no obvious dominant frequency for a particular image set, or when the dominant frequency would change with the location of the interrogation box, that image set was discarded.

F. Summary

The experiments reported on here come from an extensive measurements program over 4 years. Table I gives an indication of the number of experiments that directly contributed to each reported quantity. It does not, of course, indicate the much larger number of test and verification cases.

G. Numerical simulations

Numerical solutions of the flow field were obtained from compressible three-dimensional direct numerical simulation (DNS) using a nodal Discontinuous-Galerkin Spectral-Element Method (DGSEM) with explicit time integration. Because the focus of this paper is on experimental aspects, we only give a brief overview of the computational method and setup and refer to Ref. 37 for a more detailed description of the simulations.

In general notation, the Navier–Stokes equations can be written as a conservation law

$$\boldsymbol{Q}_t = \nabla \cdot \boldsymbol{F} \tag{4}$$

of the conserved variables

$$\boldsymbol{Q} = [\rho \quad \rho u \quad \rho v \quad \rho w \quad \rho E]^T, \tag{5}$$

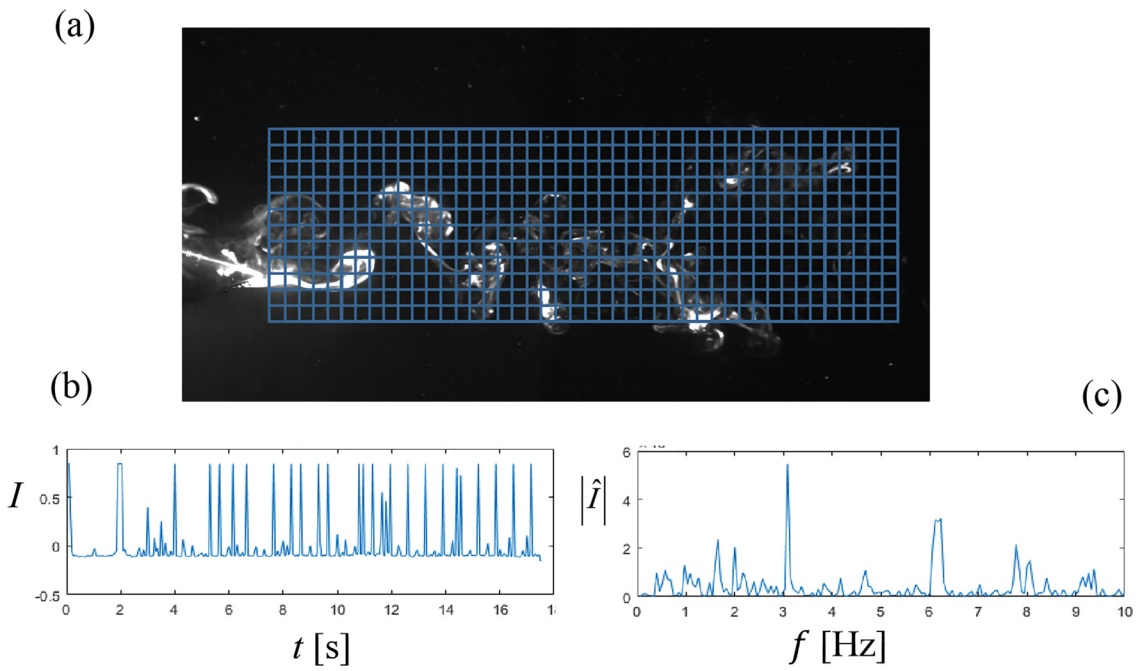

FIG. 4. (a) 20^2 pixel grid overlaid on dye visualization. (b) A time series of pixel intensities for one box. (c) Intensity power spectrum showing dominant peaks.

TABLE I. A summary of the number of experimental tests for the wind tunnel (WT) and water channel (WC), for PIV and force balance (FB) measurements, and for dye visualizations. Experiments were run over specified ranges of α, with given increments. n refers to the number of samples per α. In PIV experiments, either five or two panels cover different sections of the flow field. The FB numbers* refer to the number of sweeps through α (6), for increasing and decreasing α (2), multiplied by the number of independent experiments (at least four). Each FB average comes from 1000 data points, which are not counted. These numbers are compiled for $Re = 2 \times 10^4$ only.

Test	α range (°)	$\Delta\alpha$ (°)	n/condition	Total N
WT–PIV	[0, 10]	2	$1\,000 \times 5$	3×10^4
	[10, 11]	0.1	$1\,000 \times 2$	2×10^4
WT–FB	[−5, 11]	0.5	$2 \times 6 \times 4^*$	1688
WC–dye,	[0, 10]	0.5	400	8800
general – dye, St	[0, 8]	0.5	800	14 400

where ρ; u, v, w; and E are the density, velocity components, and inner energy, respectively, and $\boldsymbol{F}$ is the flux tensor such that

$$\nabla \cdot \boldsymbol{F} = \boldsymbol{F}_x^a + \boldsymbol{G}_y^a + \boldsymbol{H}_z^a + Re^{-1}\left(\boldsymbol{F}_x^v + \boldsymbol{G}_y^v + \boldsymbol{H}_z^v\right). \tag{6}$$

The indices a and v refer to the advective and viscous fluxes. They are defined as

$$\boldsymbol{F}^a = \begin{bmatrix} \rho u & p + \rho u^2 & \rho uv & \rho uw & u(\rho E + p) \end{bmatrix}^T, \tag{7a}$$

$$\boldsymbol{G}^a = \begin{bmatrix} \rho v & \rho vu & p + \rho v^2 & \rho vw & v(\rho E + p) \end{bmatrix}^T, \tag{7b}$$

$$\boldsymbol{H}^a = \begin{bmatrix} \rho w & \rho wu & \rho wv\, p + \rho w^2 & w(\rho E + p) \end{bmatrix}^T, \tag{7c}$$

$$\boldsymbol{F}^v = \begin{bmatrix} 0 & \tau_{xx} & \tau_{yx} & \tau_{zx} & \left(u\tau_{xx} + v\tau_{yx} + w\tau_{zx} \dfrac{\kappa}{(\gamma-1)PrM_f^2} T_x\right) \end{bmatrix}^T, \tag{8a}$$

$$\boldsymbol{G}^v = \begin{bmatrix} 0 & \tau_{xy} & \tau_{yy} & \tau_{zy} & \left(u\tau_{xy} + v\tau_{yy} + w\tau_{zy} \dfrac{\kappa}{(\gamma-1)PrM_f^2} T_y\right) \end{bmatrix}^T, \tag{8b}$$

$$\boldsymbol{H}^v = \begin{bmatrix} 0 & \tau_{xz} & \tau_{yz} & \tau_{zz} & \left(u\tau_{xz} + v\tau_{yz} + w\tau_{zz} \dfrac{\kappa}{(\gamma-1)PrM_f^2} T_z\right) \end{bmatrix}^T. \tag{8c}$$

The system of equations is closed with the equation of state,

$$p = \frac{\rho T}{\gamma M^2}. \tag{9}$$

The conservative variables in Eq. (5) are approximated in space by an Nth order polynomial within each spectral element and the fluxes are computed using a DG discretization scheme. The system of equations is integrated in time with a low-dispersion fourth-order explicit Runge– Kutta scheme. For a more detailed description of the computational method, its stability properties, and accuracy, we refer to Refs. 37–39.

The flow over a NACA 65(1)-412 airfoil was simulated at a Reynolds number based on the chord length of $Re_c = 20\,000$ and a Mach number of $M = 0.3$. The Mach number is relatively low, ensuring a nominally incompressible flow (compressibility effects on the pressure coefficient are estimated to be approximately 5% via the Prandtl–Glauert correction), but it is high enough to prevent excessively small time steps required by the explicit time integration scheme. A series of computations was conducted for angles of attack of 0°, 4°, 7°, 8°, and 10°.

The C-type grid for simulations is adopted from Ref. 40 and the outer boundaries are imposed 30 chord lengths above and below the airfoil to minimize blockage effects and spurious reflections. The computational domain is extruded by half a chord length in the spanwise direction and periodic boundary conditions are applied to model an infinite wing. The spanwise extrusion by half a chord length is in accordance with the recommendation by Almutairi *et al.*[19] The boundary elements are curved and fit to a spline representing the airfoil surface as described by Nelson *et al.*[40] The outer boundaries of the domain are defined as Riemannian freestream boundaries[41] and the airfoil surface is treated as a non-slip, adiabatic wall. Two grids are employed: a coarse grid (shown in Fig. 5) that is run with a high polynomial order of $N = 12$ in accordance with the converged solution reported by Refs. 39 and 40 and a fine grid with lower order elements ($N = 4$ for $\alpha = 7°$ and $N = 6$ for $\alpha = 8°$). The simulations on the fine grid have an overall higher wall-resolution to accommodate the turbulent flow over the airfoil surface. Because the flow at $\alpha = 10°$ is past the critical angle of attack, the coarse grid with 12th-order elements in the near field and a spectral filter is employed, which we will refer to as

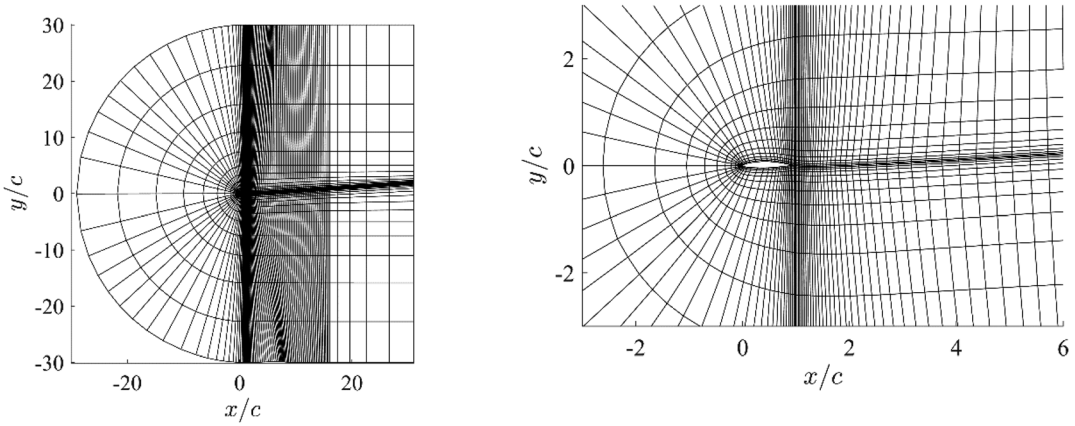

FIG. 5. Computational domain used for 3D simulations of $\alpha = 0°$, 4°, and 10°. Only elements without interior Gauss nodes shown.

TABLE II. Simulation parameters. The polynomial order = 12(1) indicates the reduced order in the far field. T_{stat} is the integration time of the flow statistics. DOF are the degrees of freedom (total number of high order nodes).

α	Grid	Polynomial order	T_{stat} $(\times U_\infty/c)$	DOF (in million)
0°	Coarse	12	10.1	74.0
4°	Coarse	12	10.2	74.0
7°	Fine	4	14.5	146.3
8°	Fine	6	8.2	401.3
10°	Coarse	12(1)	15.9	30.7

implicit large-eddy simulation (ILES).[39] Simulations at $\alpha = 0°$ and 4° are initialized with a uniform flow field and cases at $\alpha = 7°$, 8°, and 10 were initialized with results from two-dimensional computations by extruding the two-dimensional flow field along the span. All simulations are run until the flow has completely transitioned to quasi-steady state with three-dimensional structures with the statistics being recorded subsequently. A selection of key simulation parameters are given in Table II. A detailed discussion of the 2D and 3D DNS results for the NACA 65(1)-412 airfoil can be found in Ref. 37, as well as in Refs. 39 and 42.

III. RESULTS

A. Time-averaged lift and drag

The time-averaged c_l and c_d are plotted together with a modified inviscid thin airfoil prediction (starting at the experimentally determined zero lift angle of attack, α_{0L}) in Fig. 6. The lift-slope $\left(\frac{\partial c_l}{\partial \alpha} \equiv c_{l,\alpha}\right)$ is close to 2π, for small α. Note how $\alpha_{0L} > 0$ ($c_l < 0$ at $\alpha = 0°$), even when the geometric camber is positive, suggesting an effective negative camber at low α. The negative lift at $\alpha = 0°$ is caused by laminar separation over the suction surface before the trailing edge, as will be demonstrated in Secs. III B–III F. This behavior is significantly different than at a design $Re = 10^6$, where $\alpha_{0L} < 0$ and design $\alpha \approx 0$.[43] At $\alpha = 4°$, DNS and WT c_l agree and lie below the solid $2\pi\alpha$ line. The

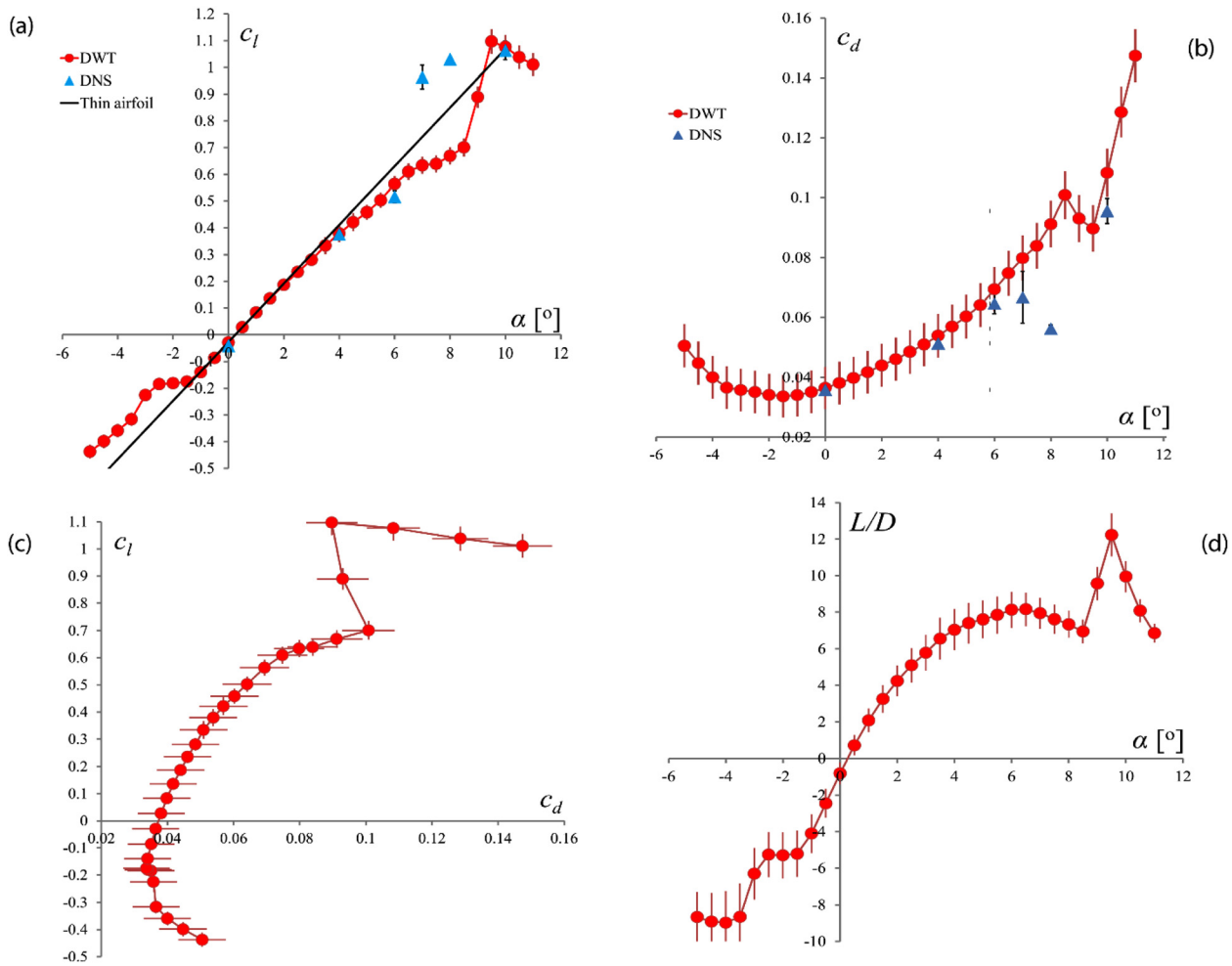

FIG. 6. Time-averaged $c_l(\alpha)$, $c_d(\alpha)$ in (a) and (b), and the polar $c_d(c_l)$ and $L/D(\alpha)$ in (c) and (d) for the NACA 65(1)-412 at $Re = 2 \times 10^4$. Experiments are in red circles, where error bars come from variation in experiments repeated day to day. DNS are in blue triangles and the error bars come from standard deviation in a time sequence.

experimental and simulation data continue to fall relative to this line until an abrupt jump in c_l occurs. This happens after $\alpha = 6°$ in the simulations and between $\alpha = 8.5°$ and $9.5°$ in experiment. In both cases, the new c_l now exceeds the $2\pi\alpha$ value. The sudden jump in c_l (and corresponding drop in c_d) comes from shifts in the separation location, and reattachment of a turbulent shear/boundary layer. The value of α when this occurs is denoted α_{crit}, and in these wind tunnel data $\alpha_{crit} = 9 \pm 0.5°$. In simulations, α_{crit} lies between $6°$ and $7°$ and this point is marked by a significant increase in standard deviation, which in simulations comes from the variation in time traces. By $\alpha = 10°$, simulations and WT c_l agree once more. The jumps in c_l and c_d are summmarized together in the lift-drag polar of Fig. 6(c) and L/D in Fig. 6(d). The $c_l(c_d)$ polar does not have a smooth c-shape as one would otherwise expect for high (design) Re. This kind of ε-shape has been noted before in airfoils at low Re,[2,21,44] and the large improvements in L/D following small increases in α suggest the potential for flow control.[22]

The principal difference between WT and DNS are the different α_{crit}. The two obvious ways in which simulation and wind tunnel experiments differ are in the end conditions of the model (no-slip walls with gaps) and in the background turbulence levels. The sensitivity to AR in experiments has been investigated, and Fig. 7 gives c_l and c_d for two wings of $AR = 3$ and 13, both at $Re = 4 \times 10^4$. Recall from Fig. 6 that $\alpha_{crit} = 9.0°$ for WT at $Re = 2 \times 10^4$. In Fig. 7, $\alpha_{crit} = 8°$ for $AR = 3$ and $\alpha_{crit} = 7°$ or $7.5°$ (depending on sweep direction) for $AR = 13$, and therefore α_{crit} is clearly a function of both Re and AR.

Since α_{crit} decreases with increasing AR, α_{crit} in any finite AR experiment may be predicted to be higher than the corresponding DNS, where the effective AR is infinite through periodic boundary conditions. Though not an explanation of why end effects are implicated this way, it does mean that PIV data derived from the $AR = 3$ wing are expected to have a higher α_{crit} than the force balance data derived from an $AR = 13$ wing in the same facility (Fig. 7). Sharp transitions between flow states around some α_{crit} have been shown and discussed by NACA 66-018,[8] all for the Eppler 387,[2,21,22] and NACA 0012.[44] As α increases from $0°$, laminar separation occurs before the trailing edge on the airfoil suction surface, and this separation point gradually moves upstream on the airfoil as α increases. At α_{crit}, the separated shear layer destabilizes and the turbulent flow reattaches, in the mean, to the airfoil. A short and thin bubble exists at around mid-chord. With a further small increase in α, the separation point moves further forward and reattachment comes from the turbulent boundary layer in the lee of the LSB. α_{crit} thus demarcates two distinct flow states: SI and SII. In SI, there is laminar separation without reattachment. In SII, the transition to turbulence in the shear layer promotes reattachment. Signatures of these transitions can be seen in the force records such as Figs. 6 and 7, and the flow states SI and SII can be observed directly in the time-averaged flow field data.

B. Flow topology—time-averaged fields

The development of the time-averaged flow before α_{crit} is shown in Fig. 8. At $\alpha = 0°$, the flow separates before the trailing edge over the suction (upper) surface. A recirculating region (v1) extends over the airfoil and aft of the trailing edge. A counter-rotating vortex (v2) appears first to originate at the trailing edge from flow around the pressure (lower) side. The net deflection of the streamlines is upward, commensurate with negative lift noted in Fig. 6. As v1 grows with increasing α, v2 is increasingly distorted and displaced downstream, appearing more as a secondary structure that is induced by v1.

Both v1 and v2 increase in size up to $\alpha = 6°$, but by $\alpha = 8°$ v1 begins to dominate the separated region, eventually, at $\alpha = 10°$, forming one large, enclosed, recirculating region that extends far beyond the trailing edge before reattachment there, as indicated by the blue line which encloses the airfoil as well as the viscous recirculating regions. The recirculating fluid has about the same cross section as the airfoil itself, and a similar vertical displacement. It could be described as a large LSB with virtual reattachment in the wake, aft of the physical trailing edge. The global flow field and streamline deflection (and hence the lift) are determined by the effective airfoil shape, made up of the combined airfoil and LSB geometry.

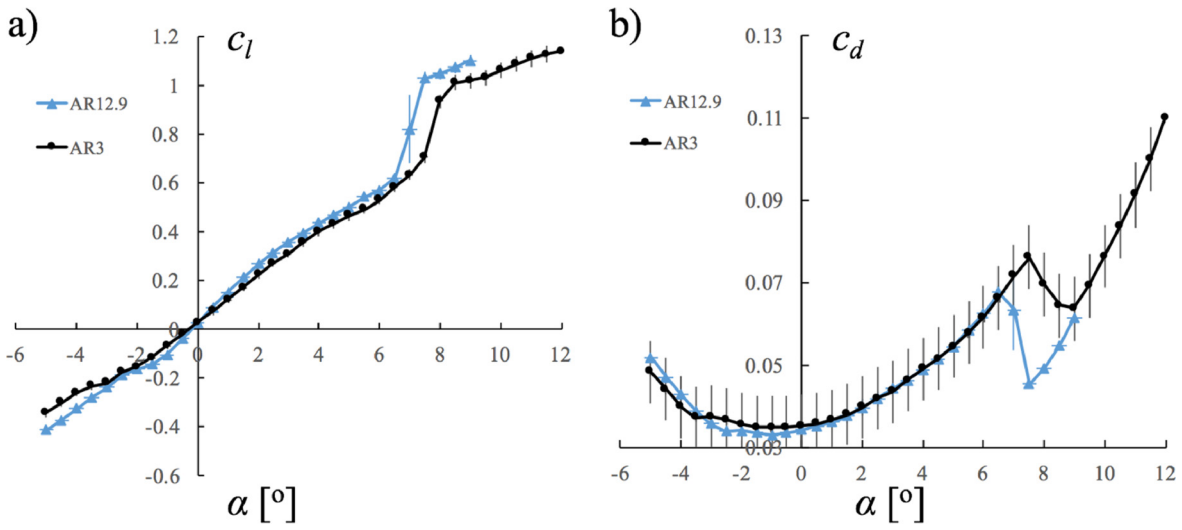

FIG. 7. $c_l(\alpha)$, $c_d(\alpha)$ in (a) and (b), at $Re = 4 \times 10^4$ for $AR = 3$ and $AR = 13$.

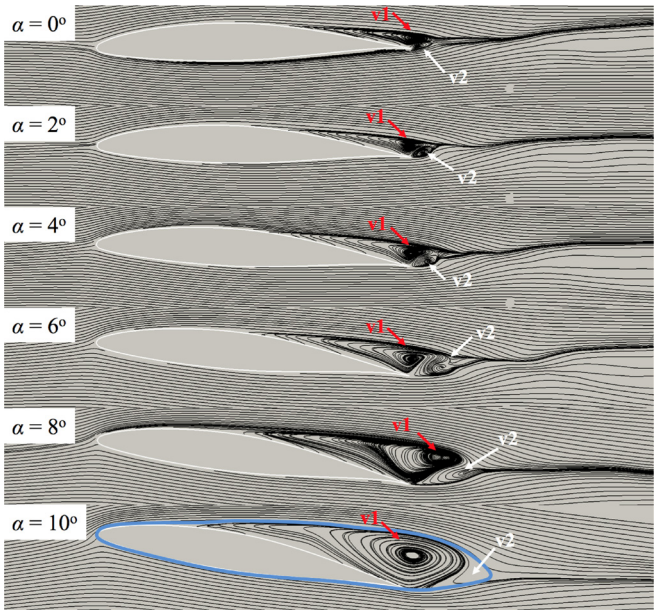

FIG. 8. Time-averaged streamlines from PIV for $\alpha < \alpha_{crit}$.

A comparison of streamlines from DNS and experiment for $\alpha = 4°$ is shown in Fig. 9, where the size and shape of v1 and v2 are similar. The counterclockwise vortex v2 originates in both cases from the pressure side of the airfoil, and forms a pair with v1. The flow at this stage is mostly two dimensional, though the clockwise v1 begins to show spanwise structure as α increases. The small differences in the shape of v1 in Fig. 9 are related to the emerging three-dimensional modes in v2, but the three-dimensional structures themselves develop downstream in the wake, after the trailing edge.

A separation streamline can be defined where locally $u = 0$ and Fig. 10 shows estimates of the location in chord-normal coordinates, $z_{n,s}$.

The data in Fig. 10 come from the most close-focused PIV experiments, which nevertheless cannot extend all the way to the wall, but the separation line is well-approximated by a straight line for $z_{n,s} < 0.15c$. At $\alpha = 10.0°$, the slow recirculating region reaches its largest size (Fig. 8) in SI. It should be noted that very small external disturbances or model vibrations will trigger the transition from SI to SII, which can occur intermittently during an inadequately controlled experiment. For

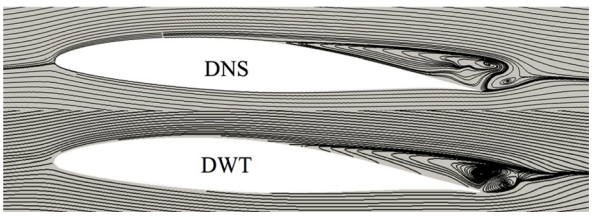

FIG. 9. Comparison of time-averaged streamlines from DNS and experiment for $\alpha = 4°$.

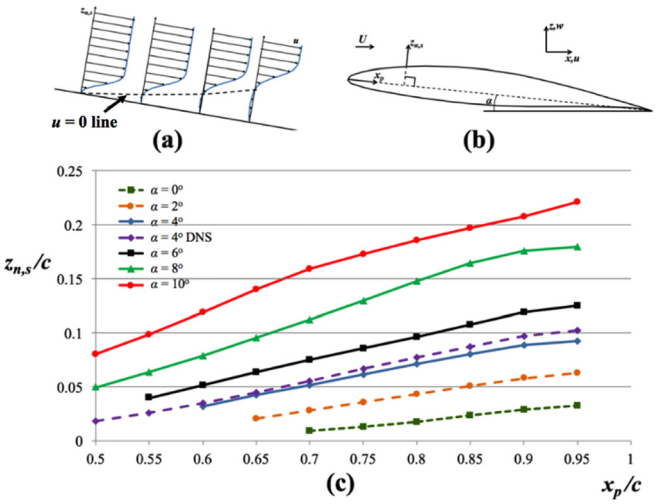

FIG. 10. (a) $u = 0$ line definition, (b) coordinate system definition, and (c) $u = 0$ line locations from PIV for $\alpha = [0° — 10°]$ and DNS $u = 0$ line location for $\alpha = 4°$.

detailed PIV experiments close to α_{crit}, model vibrations were reduced by attaching the topmost wing tip at the quarter-chord to an external mounting post, through the end plate. A representative flow convection time, $c/U = 18$ ms and a sample over 10 s thus covers approximately 530 convection times. The following PIV-derived averages were all checked for a stationary state by sub-sampling of the 1000 velocity fields. Figure 11 shows in detail the transitions around α_{crit}.

At $\alpha = 10.1°$, the flow state abruptly changes and a laminar separation bubble forms and then closes from about 1/3–2/3c. With small further increases in α, the bubble moves forward and shortens. The formation of LSB (transition from SI to SII) greatly increases the value of L/D. By driving the PIV algorithms to their local maximum resolution close to the wall, a correlation box of size 6 pixels covers 0.22 mm, which at $\alpha = 10.1°$ corresponds to about 1/8 of a bubble height. The average bubble height decreases for $\alpha = 10.2°$, and then gradually increases as the separation point moves toward the leading edge. The decrease and subsequent increase in bubble height in the time-averaged streamlines is related to the growth rate of instabilities in the separated shear layer, and the appearance of three-dimensional modes there. This will be addressed in more detail in the paper focusing on the detailed computations of flow structure.[37] The spatial resolution is sufficient to show the overall shape of the bubble, but not its internal structure, which is highly unsteady.

C. Instantaneous flow fields

The transition in flow states in Fig. 11 occurs over a small range of α, around α_{crit}. Close to α_{crit}, there can be hysteresis (depending on both AR and Re) and the bubble thickness and reattachment point can vary during a 10 s data acquisition interval. Figure 12 shows two different bubble geometries during a single run under nominally steady conditions. At $t = 1.1$ s, the separation line departs from the surface early (first measurable at approximately 8%c) and at a small angle, with transition to turbulence and reattachment at about 80%c [as shown in Fig. 12(a)]. At $t = 4.0$ s, the bubble grows much faster and the turbulent reattachment is followed by growth of the turbulent boundary

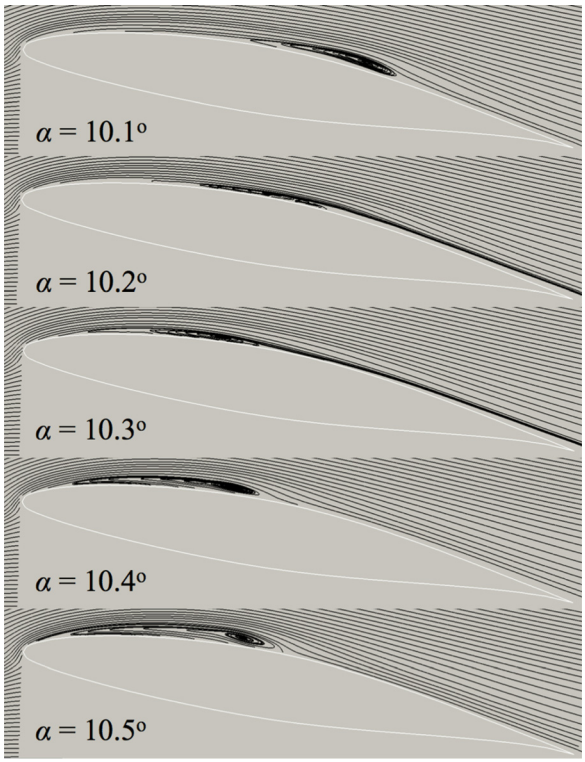

FIG. 11. Time-averaged streamlines from PIV wind tunnel experiments close to α_{crit}.

layer. This phenomenon has been termed bubble flapping[6,7,11,14,45] and is consistent with the findings of Ref. 25 that a shear layer that was farther from a wall had larger disturbance amplification rates due to a decrease in viscous damping. In general, larger amplification rates lead to earlier vortex roll-up, as observed here.

Based on the combination of instantaneous and time-averaged data from PIV in the wind tunnel and dye injection in the water channel, one can distinguish three distinct types of flow field: type (1) laminar separation with vortex roll-up beginning after the trailing edge; type (2) laminar separation with vortex roll-up beginning over the airfoil and no reattachment; and type (3) laminar separation with reattachment. Flow fields of type 1 and 2 occur before α_{crit} and are associated with the non-reattached flow state, SI, whereas type 3 occurs after α_{crit} where the flow reattaches before the trailing edge as SII. The boundary layer on the pressure side is always laminar, but with separation before the trailing edge at $\alpha = 0°$ [Fig. 13(a)]. Examples of time-averaged and instantaneous flow fields of type 1, 2, and 3 can be found in the top, middle, and bottom row, respectively, of Fig. 13.

PIV and dye injection images of the same flow type look very similar, and the measured separation locations and angles at a given α are nearly identical. The main difference is that the dye injection images show a transition from flow field type 1 to type 2 at earlier α. The earlier transition is caused by higher turbulence intensities ($T = 1.7\%$) in the water channel. When vortex roll-up occurs after the trailing edge (type 1), the primary instability mode is a wake mode

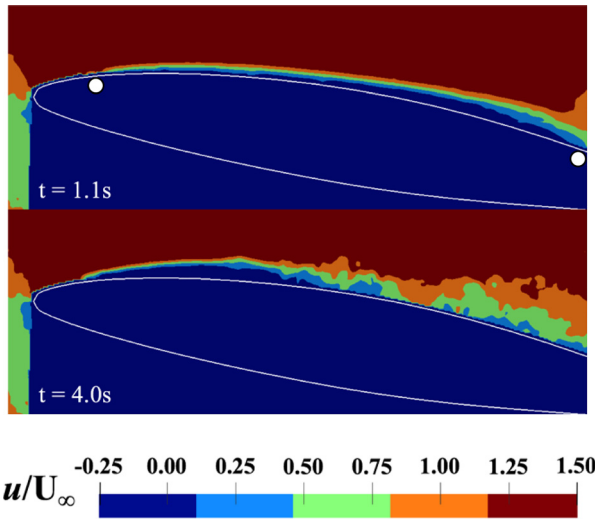

FIG. 12. The time-varying geometry of the LSB close to α_{crit}. t in seconds is from the start of a 10 s acquisition period, and no deliberate changes are made in flow conditions. $\alpha = 10.3°$, $Re = 2 \times 10^4$. The white dots mark approximate locations of separation and reattachment from time-averaged observation.

where two opposite-signed shear layers interact. With increasing α, the roll-up moves forward until it now occurs over the solid surface (type 2) and the primary instability mode is in the separated shear layer. Following transition from SI (separated without reattachment) to SII (separated with reattachment), at and after α_{crit}, the first wavy motions can be seen in the shear layer of the short laminar separation bubble. It is the rapid growth of this mode that leads to pairing and transition and a flow that is reattached, in the mean, though no instantaneous flow field resembles this mean.

D. Wake vortex shedding frequency

Wake vortex shedding frequency data from seven tests, expressed as a Strouhal number ($St = fc/U$), have been plotted for $\alpha < \alpha_{crit}$ (flow field types 1 and 2) in Fig. 14. Reliable measurements could not be made after α_{crit} because of the increased diffusion of dye before the trailing edge due to increased mixing in the reattached boundary layer when an LSB forms. St remains between 3 and 3.3 for $0° < \alpha < 3.5°$, but decreases slightly as α increases from 3.5° to 4.5° to approximately 2.6, before increasing to approximately 3.25 at $\alpha = 5°$ and remaining nearly constant until $\alpha = 8°$. Three data points for $6° < \alpha < 7°$ show St between 1.5 and 1.62, corresponding to approximately half the mean values for all other tests. The existence of prominent first subharmonics suggests a vortex pairing or merging process.

St can be determined using DNS force time traces, as wake vortex shedding causes oscillations in lift and drag. Figure 15 shows the lift and drag force oscillations over ten convective time units for the simulations at $\alpha = 4°$, 7°, and 10°. DNS St values at $\alpha = 0°$ and 4° fall within the same range as experimental data in Fig. 14, though the 7° point lies below the experimental equivalent. The time traces show numerous modes at this α.

In Fig. 14, the abrupt jump in St between $\alpha = 4.5°$ and 5° coincides with the vortex roll-up location moving upstream of the trailing

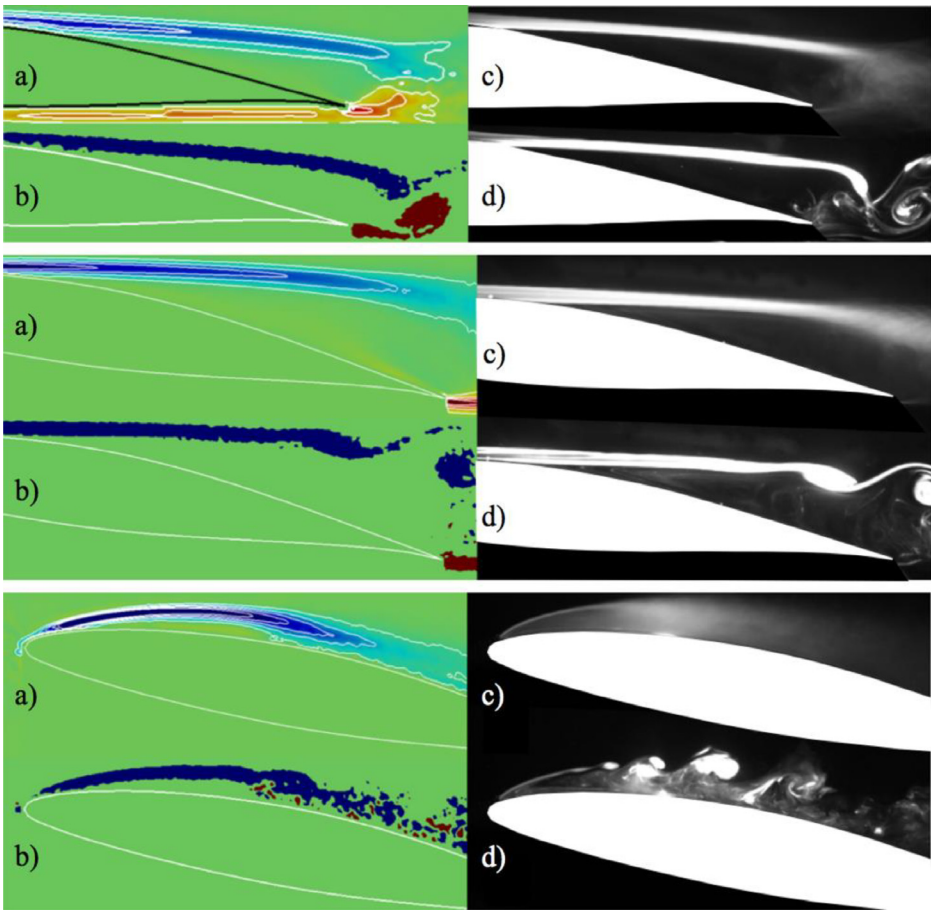

FIG. 13. (a) Time-averaged ω_y from PIV, (b) instantaneous ω_y from PIV, (c) time-averaged and (d) instantaneous dye flow visualization images for $\alpha_{PIV} = \alpha_{DFV} = 4°$ (top), $\alpha_{PIV} = 9°$ $\alpha_{DFV} = 6°$ (middle), and $\alpha_{PIV} = \alpha_{DFV} = 11°$ (bottom).

edge, which occurs at approximately $\alpha = 5.5°$. The jump in St may be due to a wake instability being replaced by a separated shear layer instability as the dominant instability mode. Reference 46 investigated vortex shedding behind a cantilevered wing at Re as low as 10^4, and found that St decreases with increasing α at a given Re, although the change in St with α was less pronounced at smaller Re. It is common to define the Strouhal number using the length of the airfoil projected in the cross-stream plane, d, as the characteristic length scale: $St^+ = fd/U$. For a NACA 0012 at $\mathrm{Re} = 2 \times 10^4$, Ref. 46 found that St^+ fell between approximately 0.3 and 0.45 at small α (0°, 2°, 5°). This matches the St^+ range found here (~0.29–0.39), for the same airfoil thickness. On the other hand, Ref. 47 found that St^+ did not vary significantly with α for a given $Re_d = Ud/\nu$ when there was laminar separation without roll-up before the trailing edge (~0.38 for a NACA 0012 at $\alpha = [0°, 2°, 3°, 3.75°]$), and then dropped when roll-up occurred before the trailing edge. Neither of these trends are obvious in the current data. In the future, we plan to investigate the use of various local length scales in or at the edge of the LSB. It is expected that the most influential length scale will change as the flow structure changes.

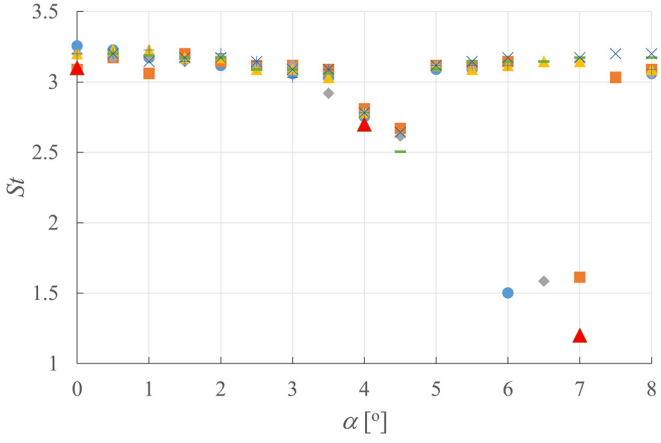

FIG. 14. St variation with α. Seven different tests are overlaid for nominally identical conditions for any given α. Red triangles show St from DNS.

E. Influence of viscosity and Reynolds number

The changes in laminar separation bubble geometry and stability have a clear and significant effect on the time-averaged and instantaneous forces and flow fields around α_{crit}, but at these Re viscous effects are important even at small α. We have noted already that at

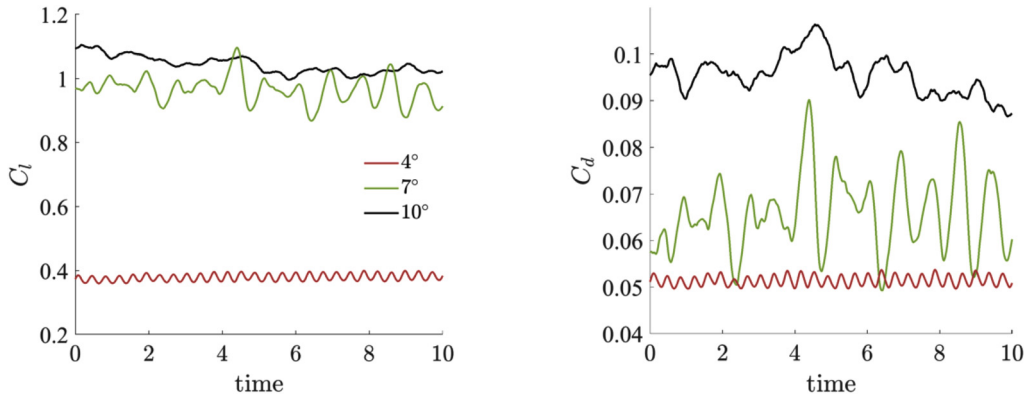

FIG. 15. Lift and drag coefficients over ten convective time units from simulations at $\alpha = 4°$, 7°, and 10°.

$Re = 2 \times 10^4$, $\alpha_{L=0} > 0$ and that this airfoil section, with positive camber, generates negative lift at $\alpha = 0°$ [Fig. 6(a)], with upward deflection of streamlines in Fig. 8. At small α, it is the surface locations of the suction and pressure side separation points that determine the aerodynamic performance,[40] and the flow is never completely attached. The effect of varying Re at small α is shown in Fig. 16.

The variation in trailing edge separation location over the suction surface is responsible for systematic Re effects at small α. As Re increases, the separation point moves aft toward the trailing edge, increasing the effective camber of the airfoil section. Now the airfoil acts as if it had positive camber for $Re = 40\,000$ and above. The lift slope at small α is 2π or greater, a surprising result that again comes from the shifting location of the trailing edge separation point. Viscous effects are commonly supposed to be detrimental to airfoil and wing performance, but in these respects they are not.

F. The combined effect of *Re*, *AR* in experiment

At high Reynolds number, neither Re nor AR would be significant parameters, but at moderate Re, they are and these sensitivities complicate interpretation among realizations (either in the literature or from the same laboratory). Experiments are described here from a number of different model geometries and facilities. The properties are summarized in Table III.

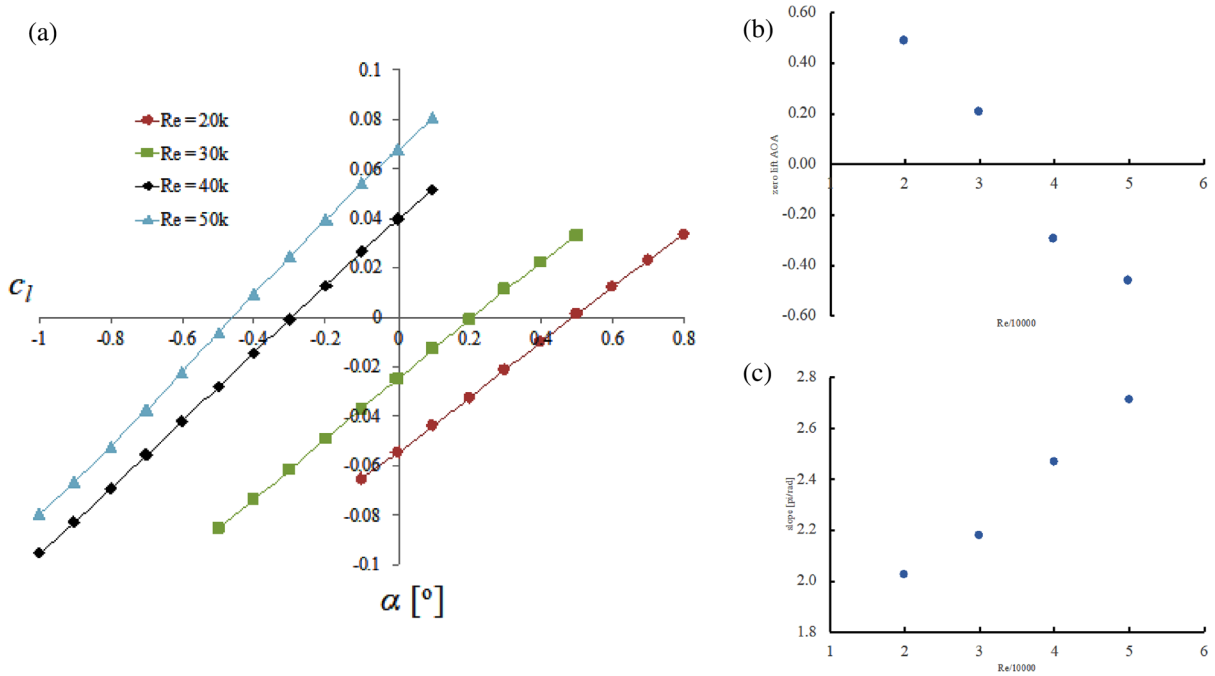

FIG. 16. (a) c_l (α) for $Re = [2, 3, 4, 5] \times 10^4$ at small α. There is a systematic decrease in $\alpha_{L=0}$ (b) and increase in $c_{l,\alpha}$ (c) with Re.

TABLE III. A summary of experiments and simulations at different *Re* and *AR*. * in simulations the span $b = 0.5c$, but boundary conditions are periodic.

Flow generator	Re ($\times 10^4$)	α_{crit} (°)	AR	Turbulence T (%U)
Numerical simulation	2	6–7	$^1/_2$ or inf*	0
Wind tunnel	2	10.1	3	0.02
		9.0	13	
	4	8	3	0.025
		7.5	13	
Water channel	2	7	3	1.7

The transition from SI to SII at α_{crit} varies with all of the parameters shown. Table I shows that α_{crit} decreases with increasing *AR*. It is well-established that *AR* affects airfoil measurements at low *Re*,[48] though for $AR < 3$, and that end-plate conditions prevent good two-dimensional approximations[49] for $Re < 10\,000$. If three-dimensional disturbances from end-plate conditions perturb the flow, a stronger influence might be expected at lower *AR*, perhaps decreasing α_{crit}. The effect is opposite, as though a three-dimensional effect were stabilizing the flow in SI. α_{crit} is lower in DNS than in the wind tunnel, and there are two principal differences: the wind tunnel has background turbulence and the simulation has periodic boundary conditions, not no-slip walls. Simulations with added background turbulence (not reported here) did not show a strong effect from the low turbulence levels obtained in this tunnel environment, and the most likely difference comes from the structures on the foil/end-plate junction. These junction flows are not included in these spanwise periodic simulations, but will be a focus of future work.

IV. CONCLUSIONS

The flow over airfoils and wings at moderate *Re* is very rich and complex with a number of qualitatively different regimes over varying α. These flow regimes are all strongly influenced by the dynamics of the viscous boundary layer, and indeed we find phenomena associated with the first four chapters of Ref. 1 all within one chord length. Two global attractors can be termed SI and SII, associated with laminar separation without and then with reattachment. In these laboratory and numerical experiments on the NACA 65-312, the progression of two-dimensional and three-dimensional instability modes leads to significant changes in the overall flow structure, as reflected in time-averaged coefficients of lift and drag. We further distinguish two regimes in SI where wake instabilities determine shedding modes (type 1) and where shear-layer instabilities occur over the upper surface (type 2) but do not cause reattachment. The transition to SII comes when the growth rate of the shear layer disturbances is sufficient for the flow to transition to turbulence, which then leads to reattachment. This study has deliberately focused on a cambered airfoil of known practical importance—even if not at these low *Re*, though there is no reason to suppose that the phenomena here are exceptional or particular to this airfoil geometry. Rather, we expect and propose that the same basic flow types, and transitions between them, will be found for many smooth and thick (>10%) airfoils and wings at moderate *Re*. There have been detailed examinations in the literature of the dynamics of the LSB itself from experiment (e.g., Refs. 7, 11, and 14) and in computations (e.g., Refs. 16–18), and these now can be placed in the full context of a flow field development that includes the initial controlling influence of the trailing edge vortex shedding from the pressure side. It will be informative to perform a detailed study of the two- and three-dimensional modes that ultimately control the global flow fields and time-averaged separation patterns discussed here.

ACKNOWLEDGMENTS

The authors are most grateful to Jack Hochschild, Ana Gabrielian, and Ethan Strijbosch for designing and running numerous water channel tests and for writing initial analysis codes.

Support from AFOSR Grant No. FA9550–16–1–0392 under Dr. Doug Smith and Dr. Gregg Abate is most gratefully acknowledged. G.B.J. acknowledges support from Solar Turbines.

DATA AVAILABILITY

The data that support the findings of this study are available from the corresponding author upon reasonable request.

REFERENCES

[1]F. M. White, *Viscous Fluid Flow*, 3rd ed. (Tata McGraw-Hill, 2011).
[2]M. S. Selig, J. J. Guglielmo, A. P. Broeren, and P. Giguere, *Summary of Low-Speed Airfoil Data* (SoarTech Publications, Virginia Beach, VA, 1995), Vol. 1.
[3]M. S. Selig, C. A. Lyon, P. Giguere, C. N. Ninham, and J. J. Guglielmo, *Summary of Low-Speed Airfoil Data* (SoarTech Publications, Virginia Beach, VA, 1996), Vol. 2.
[4]C. A. Lyon, A. P. Broeren, P. Giguere, A. Gopalarathnam, and M. S. Selig, *Summary of Low-Speed Airfoil Data* (SoarTech Publications, Virginia Beach, VA, 1998), Vol. 3.
[5]J. J. Guglielmo and M. S. Selig, "Spanwise variations in profile drag for airfoils at low Reynolds numbers," J. Aircraft **33**, 699–707 (1996).
[6]G. A. Williamson, B. D. McGranahan, B. A. Broughton, R. W. Deters, J. B. Brandt, and M. S. Selig, *Summary Low-Speed Airfoil Data* (SoarTech Publications, Virgina Beach, VA, 2012), Vol. 5.
[7]T. J. Mueller and B. J. Jansen, "Aerodynamic measurements at low Reynolds numbers," AIAA Paper No. AIAA 82-0598, 1982.
[8]T. J. Mueller and S. M. Batill, "Experimental studies of separation on a two-dimensional airfoil at low Reynolds numbers," AIAA J. **20**, 457–463 (1982).
[9]R. J. McGhee, G. S. Jones, and R. Jouty, "Performance characteristics from wind-tunnel tests of a low-Reynolds-number airfoil," in AIAA 26th Aerospace Sciences Meeting (1988)
[10]M. S. Selig and B. D. McGranahan, "Wind tunnel aerodynamic tests of six airfoils for use on small wind turbines," Report No. NREL/SR-500-34515 (National Renewable Energy Laboratory, 2004)
[11]S. Yarusevych, P. E. Sullivan, and J. G. Kawall, "Coherent structures in an airfoil boundary layer and wake at low Reynolds numbers," Phys. Fluids **18**, 044101 (2006).
[12]P. B. Lissaman, "Low-Reynolds-number airfoils," Ann. Rev. Fluid Mech. **15**, 223–239 (1983).
[13]R. Hain, C. J. Kahler, and R. Radespiel, "Dynamics of laminar separation bubbles at low-Reynolds-number aerofoils," J. Fluid Mech. **630**, 129–153 (2009).
[14]S. Burgmann and W. Schröder, "Investigation of the vortex induced unsteadiness of a separation bubble via time-resolved and scanning PIV measurements," Exp. Fluids **45**, 675–691 (2008).
[15]S. Burgmann, J. Dannemann, and W. Schröder, "Time-resolved and volumetric PIV measurements of a transitional separation bubble on an SD7003 airfoil," Exp. Fluids **44**, 609–622 (2008).
[16]L. E. Jones, R. D. Sandberg, and N. D. Sandham, "Direct numerical simulations of forced and unforced separation bubbles on an airfoil at incidence," J. Fluid Mech. **602**, 175–207 (2008).
[17]L. Jones, R. Sandberg, and N. Sandham, "Stability and receptivity characteristics of a laminar separation bubble on an aerofoil," J. Fluid Mech. **648**, 257–296 (2010).

[18]T. Sakai, P. J. Diamessis, and G. B. Jacobs, "Self-sustained instability, transition, and turbulence induced by a long separation bubble in the footprint of an internal solitary wave. I. Flow topology," Phys. Rev. Fluids **5**, 103801 (2020).
[19]J. H. Almutairi, L. E. Jones, and N. D. Sandham, "Intermittent bursting of a laminar separation bubble on an airfoil," AIAA J. **48**, 414–426 (2010).
[20]A. Uranga, P.-O. Persson, M. Drela, and J. Peraire, "Implicit large eddy simulation of transition to turbulence at low Reynolds numbers using a discontinuous Galerkin method," Int. J. Num. Methods Eng. **87**, 232–261 (2011).
[21]G. R. Spedding and J. McArthur, "Span efficiencies of wings at low Reynolds numbers," J. Aircraft **47**, 120–128 (2010).
[22]S. L. Yang and G. R. Spedding, "Separation control by external acoustic excitation at low Reynolds numbers," AIAA J. **51**, 1506–1515 (2013).
[23]S. L. Yang and G. R. Spedding, "Passive separation control by acoustic resonance," Exp. Fluids **54**, 1603 (2013).
[24]S. L. Yang and G. R. Spedding, "Local acoustic forcing of a wing at low Reynolds numbers," AIAA. J. **52**, 2867–2876 (2014).
[25]S. Yarusevych, J. G. Kawall, and P. E. Sullivan, "Separated-shear-layer development on an airfoil at low Reynolds numbers," AIAA J. **46**, 3060–3069 (2008).
[26]S. Yarusevych, P. E. Sullivan, and J. G. Kawall, "On vortex shedding from an airfoil in low-Reynolds-number flows," J. Fluid Mech. **632**, 245–271 (2009).
[27]T. M. Kirk and S. Yarusevych, "Vortex shedding within laminar separation bubbles forming over an airfoil," Exp. Fluids **58**, 43 (2017).
[28]M. S. Istvan and S. Yarusevych, "Effects of free-stream turbulence intensity on transition in a laminar separation bubble formed over an airfoil," Exp. Fluids **59**, 52 (2018).
[29]O. Marxen and D. S. Henningson, "The effect of small-amplitude convective disturbances on the size and bursting of a laminar separation bubble," J. Fluid Mech. **671**, 1–33 (2011).
[30]O. Marxen, M. Lang, and U. Rist, "Vortex formation and vortex breakup in a laminar separation bubble," J. Fluid Mech. **728**, 58–90 (2013).
[31]P.-L. Delafin, F. Deniset, and J.-A. Astolfi, "Effect of the laminar separation bubble induced transition on the hydrodynamic performance of a hydrofoil," Eur. J. Mech.-B/Fluids **46**, 190–200 (2014).
[32]J. B. Barlow, W. H. Rae, and A. Pope, *Low-Speed Wind Tunnel Testing*, 3rd ed. (Wiley, New York, 1999)
[33]G. R. Spedding and E. J. Rignot, "Performance analysis and application of grid interpolation techniques for fluid flows," Exp. Fluids **15**, 417–430 (1993).
[34]A. M. Fincham and G. R. Spedding, "Low-cost, high resolution DPIV for measurement of turbulent fluid flow," Exp. Fluids **23**, 449–462 (1997).
[35]M. Zabat, S. Farascaroli, F. K. Browand, M. Nestlerode, and J. Baez, "Drag measurements on a platoon of vehicles," *California Partners for Advanced Transit and Highways* (University of California, Berkeley, California, 1994).
[36]W. Kester, "ADC input noise: The good, the bad, and the ugly. Is no noise good noise?" Analog Dialogue **40**, 2 (2006).
[37]B. F. Klose, G. R. Spedding, and G. B. Jacobs, "Direct numerical simulation of cambered airfoil aerodynamics at Re = 20 000," arXiv:2108.04910.
[38]D. A. Kopriva, *Implementing Spectral Methods for Partial Differential Equations* (Springer, New York, 2009).
[39]B. F. Klose, G. B. Jacobs, and D. A. Kopriva, "Assessing standard and kinetic energy conserving volume fluxes in discontinuous Galerkin formulations for marginally resolved Navier-Stokes flows," Comput. Fluid **205**, 104557 (2020).
[40]D. A. Nelson, G. B. Jacobs, and D. A. Kopriva, "Effect of boundary representation on viscous, separated flows in a discontinuous-Galerkin Navier-Stokes solver," Theor. Comput. Fluid Dyn. **30**, 363–385 (2016).
[41]G. B. Jacobs, D. A. Kopriva, and F. Mashayek, "A comparison of outflow boundary conditions for the multidomain staggered-grid spectral method," Numer. Heat Transfer, Part B **44**, 225–251 (2003).
[42]B. F. Klose, G. B. Jacobs, J. Tank, and G. R. Spedding, "Low Reynolds number airfoil aerodynamics: Three different flow patterns within an angle of attack range of four degrees," Bull. Am. Phys. Soc. **63**, D32.00008 (2018).
[43]I. H. Abbot and A. E. von Doenhoff, *Theory of Wing Sections Including a Summary of Airfoil Data* (General Publishing Company, Toronto, 1959), p. 622.
[44]J. Tank, L. Smith, and G. R. Spedding, "On the possibility (or lack thereof) of agreement between experiment and computation of flows over wings at moderate Reynolds number," J. R. Soc. Interface. **7**, 20160076 (2017).
[45]W. Zhang, R. Hain, and C. Kahler, "Scanning PIV investigation of the laminar separation bubble on a SD7003 airfoil," Exp. Fluids **45**, 725–743 (2008).
[46]R. F. Huang and C. L. Lin, "Vortex shedding and shear-layer instability of wing at low-Reynolds numbers," AIAA J. **33**, 1398–1403 (1995).
[47]R. F. Huang and H. W. Lee, "Turbulence effect on frequency characteristics of unsteady motions in wake of wing," AIAA J. **38**, 87–94 (2000).
[48]A. Pelletier and T. J. Mueller, "Low Reynolds number aerodynamics of low-aspect-ratio, thin/flat/cambered-plate wings," J. Aircraft **37**, 825–832 (2000).
[49]A. Pelletier and T. J. Mueller, "Effect of endplates on two-dimensional airfoil testing at low Reynolds number," J. Aircraft **38**, 1056–1059 (2001).